

Supporting Information for
Origins of Near-Infrared-II Emission Tail and Fluorescence
Enhancement of the Albumin-chaperoned Cyanine Dyes from a
Multiscale Computational Study

**Guanyu Jiang¹, Zhubin Hu¹, Lang Bai², Cheng Zhong³, Sen Lu^{4,5}, Baoshan Han^{4,5},
Zhenrong Sun¹, Shoujun Zhu², Yongye Liang⁶ and Haitao Sun^{1,7,8*}**

¹ *State Key Laboratory of Precision Spectroscopy, School of Physics and Electronic
Science, East China Normal University, Shanghai 200241, China*

² *State Key Laboratory of Supramolecular, Structure and Material College of Chemistry, Jilin
University, Changchun 130012, China*

³ *Hubei Key Lab on Organic and Polymeric Optoelectronic Materials, Department of
Chemistry, Wuhan University, Wuhan 430072, China*

⁴ *Department of General Surgery, Xinhua Hospital, Affiliated with Shanghai Jiao Tong
University School of Medicine, Shanghai 200092, China*

⁵ *School of Health Science and Engineering, University of Shanghai for Science and
Technology, Shanghai 200093, China*

⁶ *Department of Materials Science and Engineering, Shenzhen Key Laboratory of Printed
Organic Electronics, Southern University of Science and Technology, Shenzhen 518055,
China*

⁷ *Collaborative Innovation Center of Extreme Optics, Shanxi University, Taiyuan,
Shanxi, 030006, China*

⁸ *NYU-ECNU Center for Computational Chemistry at NYU Shanghai, Shanghai,
200062, China*

* Corresponding Authors Email: htsun@phy.ecnu.edu.cn (H.S.)

Contents

1. Experimental section	S1
2. Computational Details	S1
Table S1. Calculated emission wavelengths (λ , nm) and oscillator strengths (f) of ICG and IR783 using different levels of theory based on their planar structures of excited state.	S4
Table S2. The relative energies (ΔE , kcal/mol) between the planar ($\sim 0^\circ$) and TICT ($\sim 90^\circ$) structures for ICG and IR783 calculated by different DFT methods.	S4
Table S3. Calculated bond lengths (B3) of ICG*, ICG and IR783 in both ground- (S_0) and first excited (S_1) state.	S5
Figure S1. Chemical structures of ICG and IR783; The top 10 conformations with highest scores after docking were sorted.; calculated potential energy surface (kcal/mol) as a function of dihedral angle of D3 through fitting parameters in comparison with the calculated PES by quantum chemical (QC) calculations.	S5
Figure S2. Calculated potential energy surface (PES) of lowest singlet excited states (S_1) as a function of dihedral angles of D1, D2, D3 and D4 for ICG and IR783.	S6
Figure S3. The simulated vibrationally resolved emission spectra of ICG and IR783 based on their planar structures.	S7
Figure S4. The HR factors versus normal vibration modes for ICG and IR783 in water.	S7
Figure S5. Analysis of average noncovalent interactions (aNCI) between BSA and ICG / IR783 The root means square deviation (RMSD) of ICG-BSA and IR783-BSA collected based on the last 10 ns MD trajectories.	S8
Figure S6. Measured fluorescence enhancement ratio by comparing the fluorescence intensity in NIR-I region versus NIR-II region for ICG and IR783 in BSA solutions. Measured fluorescence enhancement ratio between the NIR-I fluorescence intensity of IR783 and ICG, as well as their NIR-II intensity.	S8
Figure S7. Distribution probability of dihedral angles of D1 and D4 of free IR783 and IR783-BSA in water collected based on the last 10 ns MD trajectories; The number of water molecules (N_{H_2O}) within the first solvent shell of free-IR783 and BSA-IR783 as a function of simulation time.	S9
Figure S8. 10 sample structures selected from MD simulations after equilibrium.	S9
References of SI	S10

1. Experimental section

1.1 Materials

The dye of ICG was purchased from TCI (Shanghai) Development Co., Ltd. The dye of IR-783 and bovine serum albumin were purchased from Sigma-Aldrich.

1.2 Cyanine in protein solution

BSA was dissolved in $1 \times$ PBS with a concentration of 10 mg/mL (150 μ M). IR-783 was dissolved in dimethyl sulfoxide (DMSO) at 2 mM. For a typical reaction, 50 μ L of IR-783 was added into the 667 μ L BSA solutions with 283 μ L of PBS. Then, the mixed solution was vortexed for 10 seconds.

1.3 NIR-II imaging

The excitation laser was an 808-nm laser set-up at a power density of 65 mW/cm². NIR-I and NIR-II emission fluorescence were respectively collected with a combination of 850 nm long-pass and 1000 nm short-pass filters, and 1000 nm long-pass and 1300 nm short-pass filters. A definite exposure time (4 ms) was used for the InGaAs camera to capture images in the NIR-I and NIR-II window.

2. Computational Details

2.1 Quantum chemical calculations.

We also benchmarked the calculations of emission wavelengths by different methods: (i) TDDFT with various hybrid and range-separated hybrid functionals (LC-BLYP*, ω B97XD*, LC-BLYP, ω B97XD, PBE0, and CAM-B3LYP)¹⁻³; (ii) the second-order approximate coupled-cluster (CC2) method, the second-order algebraic diagrammatic construction [ADC(2)] approach and its spin-component scaled (SCS) version [SCS-ADC(2)]; (iii) CIS(D)-based double hybrid TDDFT (DSD-PBEP86/CIS(D)).⁴ All the aforementioned DFT calculations with 6-311G(d) basis set and PCM solvation model were carried out by Gaussian 16 software and the double hybrid TDDFT and second-order CC2/ADC(2) calculations were performed with def2-TZVP basis set⁵ in the gas phase by MRCC 2022 program. The vibrationally-resolved electronic emission spectra of organic dyes were simulated by Franck-Condon⁶ and

Herzberg-Teller (FCHT) approximation⁷ to study the vibrational effect on NIR-II tail emission using Gaussian 16 software. An ensemble of 500 nuclear geometries was generated according to the finite-temperature uncorrelated Wigner distribution based on the harmonic vibrational analysis of the first excited state under 0 or 300 K temperature for the nuclear ensemble approach (NEA).

2.2 Docking modeling

The scoring function includes the effects of Gaussian steric interaction terms, finite repulsion terms, etc., and the optimization algorithm is iterated local search global optimizer^{8,9} consisting of a mutation and a local optimization. The “exhaustiveness” parameter corresponding to the number of runs of the search was set to 100 to allow for sufficient search space. In the experiment, the cyanine ligand has strong interactions with docking pocket DI (protein domain) and DIII, but has almost no interaction with DII, making the ligand docked to the hydrophobic pocket of BSA as shown in Figure. S1d. Thus, the molecular docking structure of the complex with the highest score was selected for the following MD simulation (Figure S1c).

2.3 Molecular dynamics simulations

During the simulation, all bonds with hydrogen atoms were fixed using the linear constraint solver (LINCS) algorithm.¹⁰ The particle mesh Ewald (PME)¹¹ method with a 1 nm cutoff in real space was used to calculate the electrostatic interactions. The cutoff for the nonbonding van-der Waals interactions was set to be 1 nm. The velocity-rescale thermostat¹² with a coupling time of 0.2 ps was used to regulate temperature. The Berendsen barostat¹³ with a time constant of 0.5 ps for the equilibration simulation and the Parrinello-Rahman barostat¹⁴ with a time constant of 2 ps for the production simulation was used to maintain the pressure to 1 bar. The initial geometry of organic dye was optimized at the same B3LYP/6-311G(d) level and then the resulting restrained electrostatic potential (RESP2) charges¹⁵ were obtained by Multiwfn 3.7 code and the General Amber Force Field (GAFF)¹⁶ obtained via ACPYPE tool¹⁷ were assigned for the optimized structure. The AMBER99SB-ILDN¹⁸ force field is used for BSA protein whose structure was taken from RCSB Protein Data Bank (PDB ID: 4F5S).^{19, 20}

The initial structure of the protein-cyanine complex was immersed in the center of a $16.5 \times 16.5 \times 16.5 \text{ nm}^3$ cubic box of TIP3P²¹ water molecules, and all of the solute atoms were no less than 0.8 nm from the boundary of the water box.

Notably, the dihedral angle parameter has a great influence on the conformation of a single molecule and the resulting trajectory in dynamics, and the dihedral angle given by the classic force field through the atomic type may be inaccurate. Therefore, when simulating flexible molecules, it is usually necessary to optimize the dihedral angle to obtain more accurate molecular conformation. To obtain more accurate molecular conformations for excited states, the parameters of dihedral angle were optimized by our home-built zTOP code²² based on the excited-state potential energy surface (PES) at the LC-BLYP*²³/6-311G(d) level. The optimized parameters of dihedral angle can reasonably predict the TICT structure of dyes (Figure S1, e and f) while the default GAFF parameters fail.

2.4 Binding free energy calculation

Within MM/GBSA method, the binding free energy can be represented as

$$\langle \Delta G_{bind} \rangle = \langle \Delta H \rangle - \langle T\Delta S \rangle = \langle \Delta E_{gas} \rangle + \langle \Delta G_{sol} \rangle - \langle T\Delta S \rangle$$

Herein, $\langle \dots \rangle$ means the ensemble average; the ΔG_{bind} is the binding free energy; ΔH is the enthalpy of binding; $-T\Delta S$ is the conformational entropy after cyanine dyes binding; ΔE_{gas} denotes the difference of gas-phase energy between that of the protein-cyanine complex and those of the separate protein and cyanine ligand, and is computed by MM method; ΔG_{sol} is the difference of solvation free energy between that of the protein-cyanine complex and those of the separate protein and cyanine systems, and is computed by GBSA method. To compute $\langle \Delta G_{bind} \rangle$, a separate MD run for 1 ns with a configurational sampling frequency of 100 fs was performed and a total of 10000 snapshots were extracted from the MD trajectories for the calculation of binding free energy. It should be noted that the entropic term $-T\Delta S$ is not included in our binding free energy and thus the relative binding free energies correspond to the enthalpy of binding $\langle \Delta H \rangle$ that is usually sufficient for comparing relative binding free energies of related ligands.²⁴

Table S1. Calculated emission wavelengths (λ , nm) and oscillator strengths (f) of ICG and IR783 using different levels of theory based on their planar structures of excited state. ω represents the optimally-tuned parameters for range-separated hybrid functionals (bohr⁻¹).

Theory	Basis set	Solvation model	ICG			IR783		
			ω	λ	f	ω	λ	f
LC-BLYP*	6-311G(d)	PCM	0.072	820	2.58	0.075	789	2.49
ω B97XD*	6-311G(d)	PCM	0.044	754	2.76	0.048	744	2.61
LC-BLYP	6-311G(d)	PCM		729	2.80		764	2.58
ω B97XD	6-311G(d)	PCM		726	2.80		744	2.56
PBE0	6-311G(d)	PCM		749	2.78		736	2.62
CAM-B3LYP	6-311G(d)	PCM		724	2.81		739	2.59
CC2	def2-TZVP	GAS		733			689	
ADC(2)	def2-TZVP	GAS		898			851	
SCS-ADC(2)	def2-TZVP	GAS		803			780	
DSD-PBEP86/CIS(D)	def2-TZVP	GAS		755			714	
Exp*	///	///		822/1400			805/1400	

Table S2. The relative energies (ΔE , kcal/mol) between the planar ($\sim 0^\circ$) and TICT ($\sim 90^\circ$) structures for ICG and IR783 calculated by different DFT methods. Δ : the energy difference of ΔE of TICT structures for ICG and IR783.

Theory (DFT/6311G(d)/PCM)	ICG		IR783		Δ
	Planar	TICT	Planar	TICT	
B3LYP	0	+6.6 kcal/mol	0	+0.8 kcal/mol	5.8 kcal/mol
PBE0	0	+9.4 kcal/mol	0	+3.9 kcal/mol	5.5 kcal/mol
ω B97XD*	0	+9.4 kcal/mol	0	+3.1 kcal/mol	6.3 kcal/mol
LC-BLYP*	0	+2.0 kcal/mol	0	-1.9 kcal/mol	3.9 kcal/mol

Table S3. Calculated bond lengths (B3) of ICG*, ICG and IR783 in both ground- (S_0) and first excited (S_1) state.

B3 (Å)	ICG*	ICG	IR783
S_0	1.396	1.396	1.402
S_1	1.399	1.397	1.407

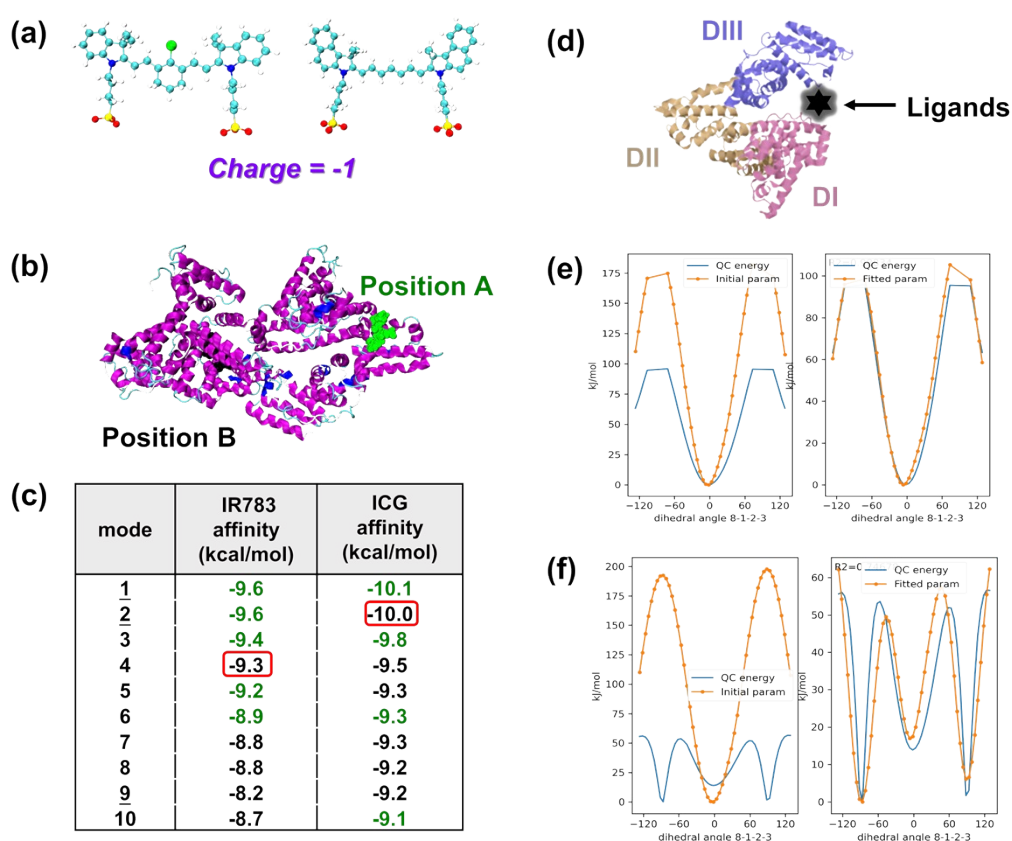


Figure S1. (a) Chemical structures of ICG and IR783; (b, c) The top 10 conformations with highest scores after docking were sorted. And they were divided into two categories (position A, Green and position B, Black) according to their preferred binding positions (b); (c) the black star symbol represents the most possible binding position of ligands observed in experiment (d) calculated potential energy surface (kcal/mol) as a function of dihedral angle of D3 through fitting parameters in comparison with the calculated PES by quantum chemical (QC) calculations, and the parameter fitting for ground states

(e) and excited states (f).

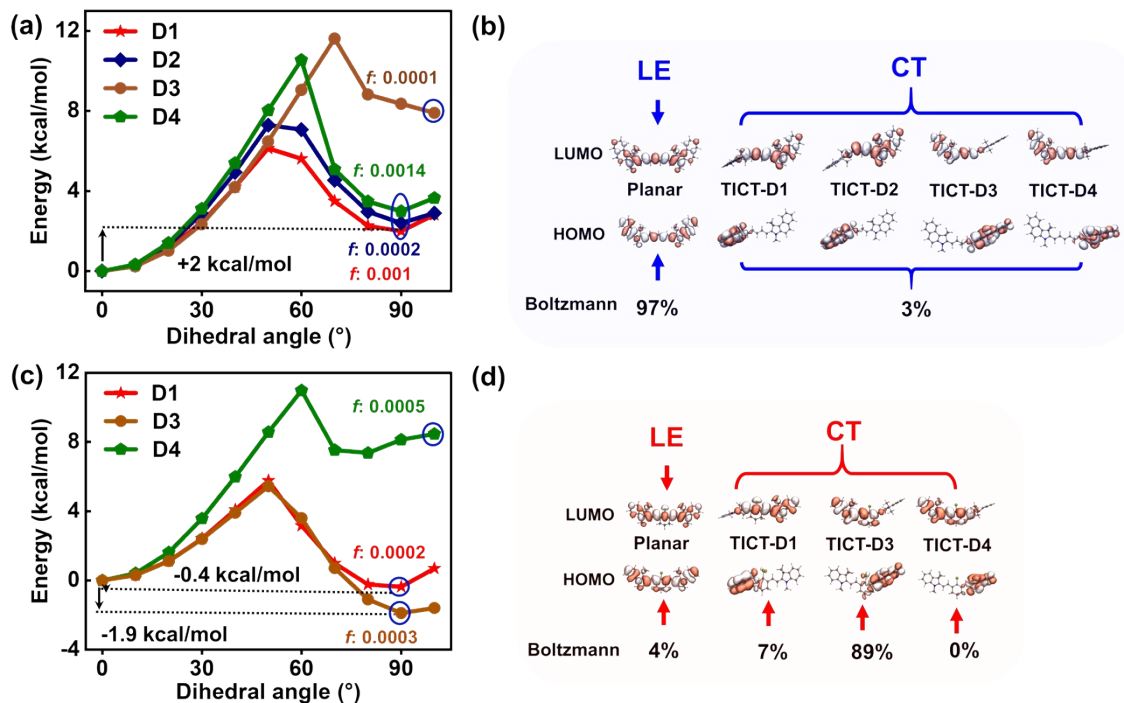


Figure S2. Calculated potential energy surface (PES) of lowest singlet excited states (S_1) as a function of dihedral angles of D1, D2, D3 and D4 for ICG (a) and IR783 (c), the energy gaps between planar structure and TICT structure, as well as the oscillator strength of TICT structure are also listed. The HOMO and LUMO distributions based on their planar and TICT structures (blue circles in Figure S2a and S2c) of S_1 states for ICG (b) and IR783 (d).

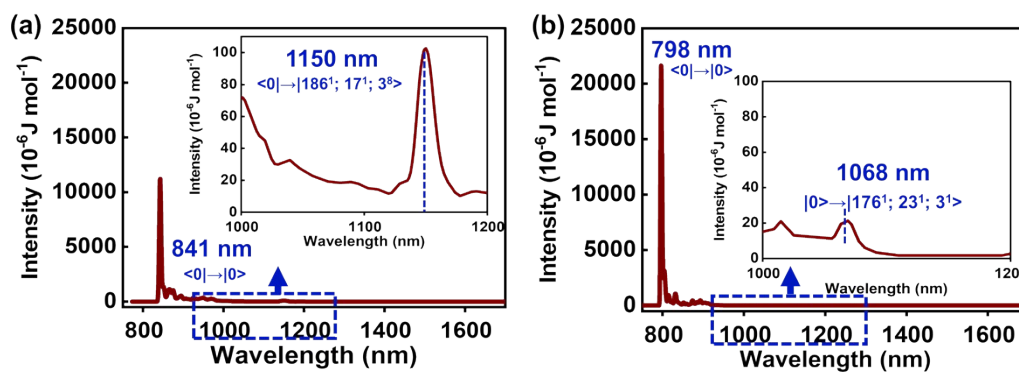


Figure S3. The simulated vibrationally resolved emission spectra of ICG (a) and IR783 (b) based on their planar structures.

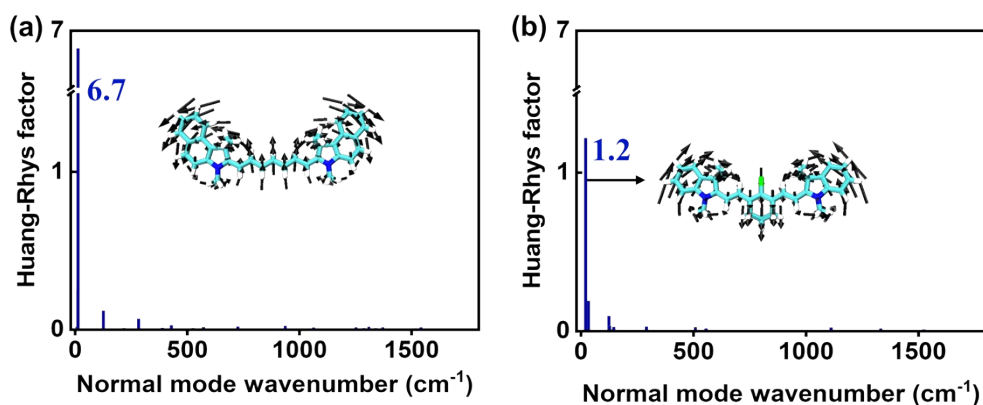


Figure S4. The HR factors versus normal vibration modes for ICG (a) and IR783 (b) in water, the vibration mode which contributes the most to HR factors are also inserted.

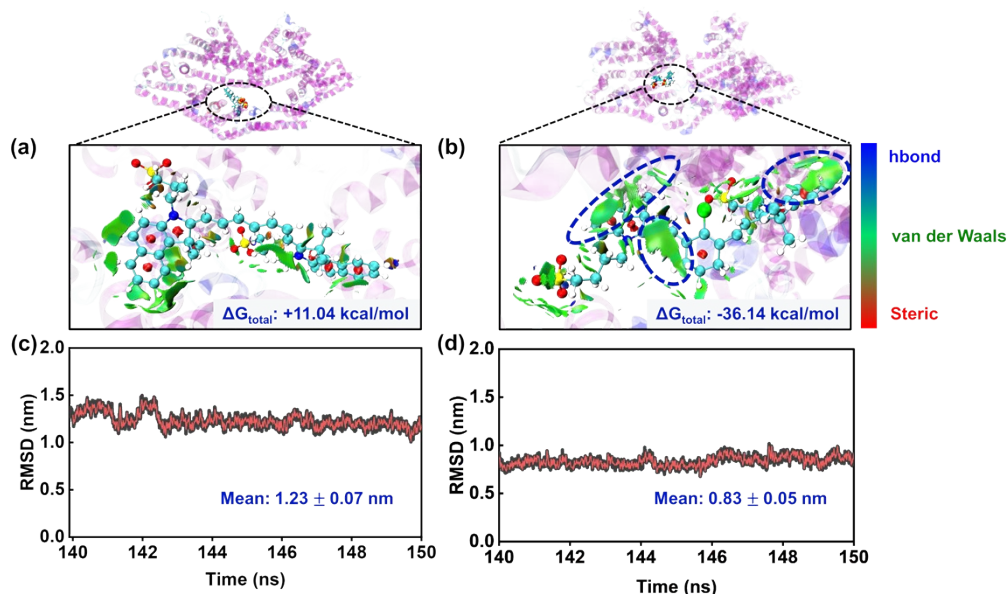


Figure S5. Analysis of average noncovalent interactions (aNCI) between BSA and ICG (a) / IR783 (b), the calculated binding free energies (ΔG_{total}) of the protein-cyanine complex are also listed. The root mean square deviation (RMSD) of ICG-BSA (c) and IR783-BSA (d) collected based on the last 10 ns MD trajectories, the mean values of RMSD are also listed.

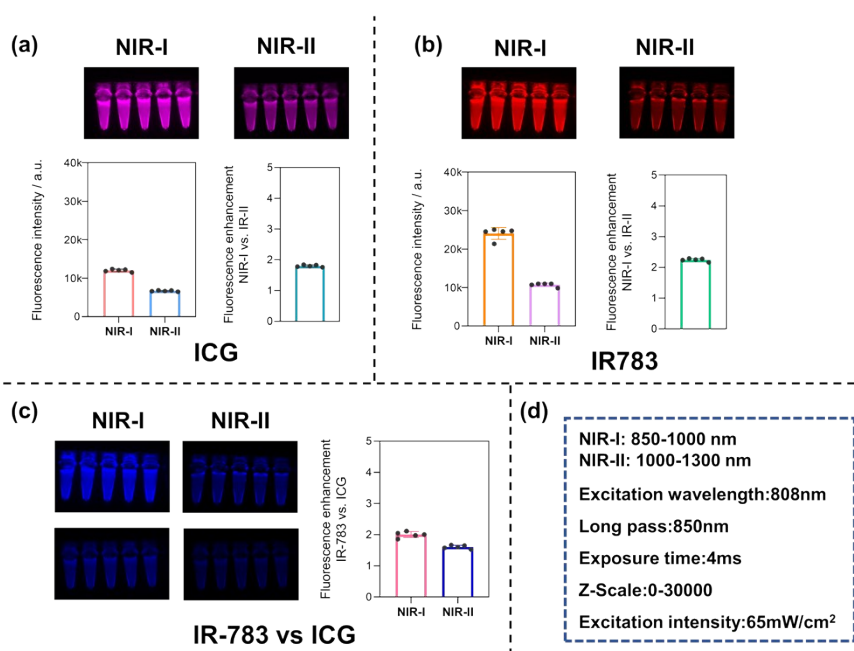


Figure S6. (a) Measured fluorescence enhancement ratio by comparing the fluorescence intensity in NIR-I region versus NIR-II region for ICG (a) and IR783 (b) in BSA solutions. (c) measured fluorescence enhancement ratio between the NIR-I fluorescence intensity of IR783 and ICG, as well as their NIR-II intensity.

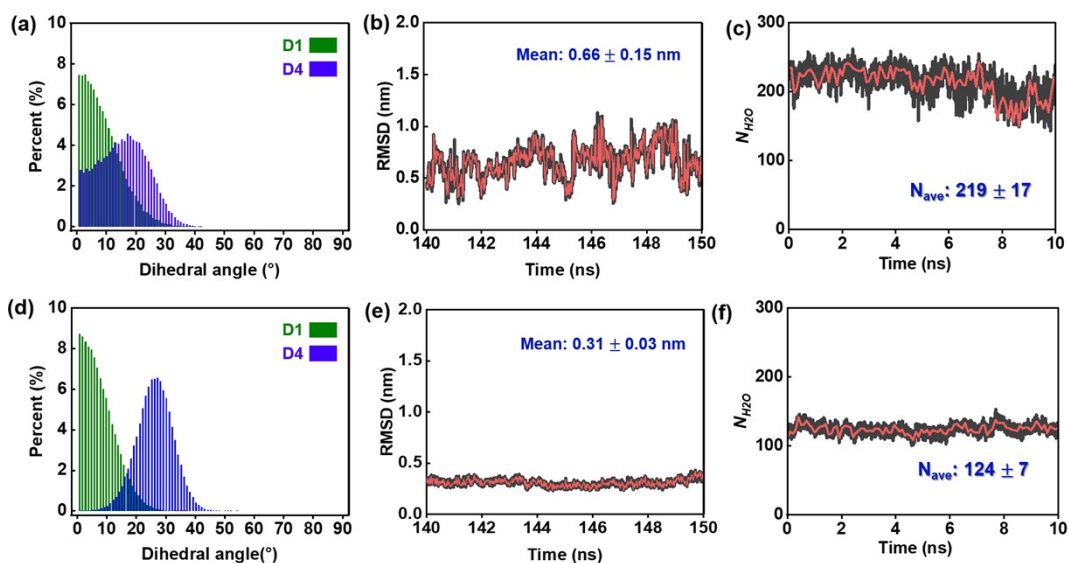


Figure S7. Distribution probability of dihedral angles of D1 (olive) and D4 (blue) of free IR783 (a) and IR783-BSA (d) in water collected based on the last 10 ns MD trajectories; The root means square deviation (RMSD) of free IR783 (b) and IR783-BSA (e) in the last 10 ns MD simulations, the mean RMSD value is also listed; The number of water molecules (N_{H_2O}) within the first solvent shell of free-IR783 (c) and BSA-IR783 (f) as a function of simulation time. The average number of water molecules is listed.

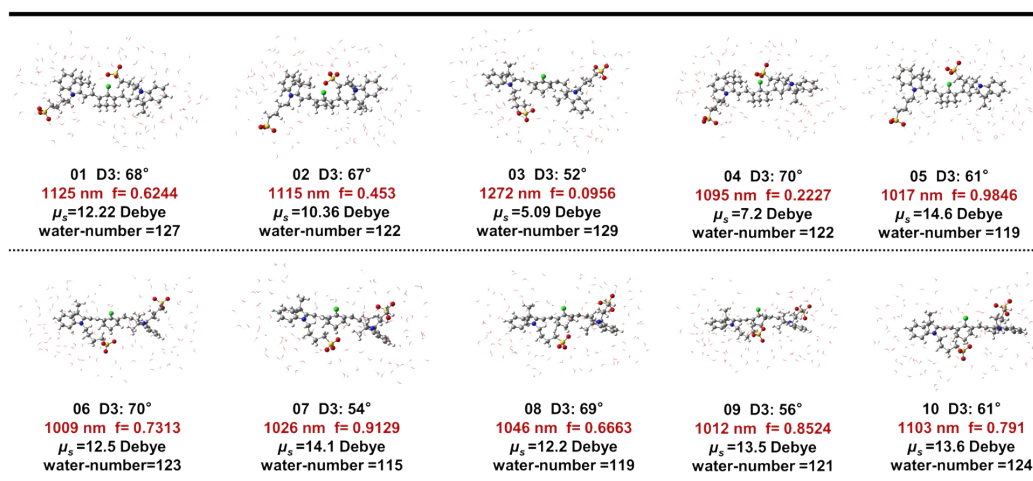


Figure S8. 10 sample structures selected from MD simulations after equilibrium, and their corresponding dihedral angles of D3 are distributed between 50° and 70°, resembling the structures maintained in BSA. These selected sample structures possess NIR-II emission wavelength, and moderate oscillator strengths are also inserted.

References

- (1) Chai, J.-D., Head-Gordon, M. Long-range corrected hybrid density functionals with damped atom–atom dispersion corrections. *Phys. Chem. Chem. Phys.* **2008**, *10*, 6615-6620.
- (2) Adamo, C., Barone, V. Toward reliable density functional methods without adjustable parameters: The PBE0 model. *J. Chem. Phys.* **1999**, *110*, 6158-6170.
- (3) Yanai, T.; Tew, D. P., Handy, N. C. A new hybrid exchange–correlation functional using the Coulomb-attenuating method (CAM-B3LYP). *Chem. Phys. Lett.* **2004**, *393*, 51-57.
- (4) Kozuch, S., Martin, J. M. L. DSD-PBEP86: in search of the best double-hybrid DFT with spin-component scaled MP2 and dispersion corrections. *Phys. Chem. Chem. Phys.* **2011**, *13*, 20104.
- (5) Weigend, F., Ahlrichs, R. Balanced basis sets of split valence, triple zeta valence and quadruple zeta valence quality for H to Rn: Design and assessment of accuracy. *Phys. Chem. Chem. Phys.* **2005**, *7*, 3297-3305.
- (6) Condon, E. U. Nuclear motions associated with electron transitions in diatomic molecules. *Phys. Rev.* **1928**, *32*, 858-872.
- (7) G, H. E., Teller, Z. *Z. Physik. Chern. (Leipzig)* **1933**, *B21*, 410.
- (8) Baxter, J. *Oper. Res. Soc.* **1981**, *32*, 815.
- (9) Blum, A. R. C. B., M.; Sampels, M. Eds. *Hybrid metaheuristics: an emerging approach to optimization; springer-verlag,:* Berlin, Heidelberg, 2008.
- (10) Hess, B.; Bekker, H.; Berendsen, H. J. C., Fraaije, J. G. E. M. LINCS: A linear constraint solver for molecular simulations. *J. Comput. Chem.* **1997**, *18*, 1463-1472.
- (11) Essmann, U.; Perera, L.; Berkowitz, M. L.; Darden, T.; Lee, H., Pedersen, L. G. A smooth particle mesh Ewald method. *J. Chem. Phys.* **1995**, *103*, 8577-8593.
- (12) Bussi, G.; Donadio, D., Parrinello, M. Canonical sampling through velocity rescaling. *J. Chem. Phys.* **2007**, *126*, 014101.
- (13) Berendsen, H. J. C.; Postma, J. P. M.; van Gunsteren, W. F.; DiNola, A., Haak, J. R. Molecular dynamics with coupling to an external bath. *J. Chem. Phys.* **1984**, *81*, 3684-3690.
- (14) Abascal, J. L., Vega, C. A general purpose model for the condensed phases of water: TIP4P/2005. *J. Chem. Phys.* **2005**, *123*, 234505.
- (15) Voci, S.; Zinna, F.; Arrico, L.; Grass, S.; Bouffier, L.; Lacour, J.; Di Bari, L., Sojic, N. Chiroptical detection of a model ruthenium dye in water by circularly polarized-electrochemiluminescence. *Chem. Commun.* **2020**, *56*, 5989-5992.
- (16) Wang, J.; Wolf, R. M.; Caldwell, J. W.; Kollman, P. A., Case, D. A. Development and testing of a general amber force field. *J. Chem. Phys.* **2004**, *25*, 1157-1174.
- (17) Sousa da Silva, A. W., Vranken, W. F. ACPYPE - AnteChamber PYthon Parser interfacE. *BMC. Research. Notes.* **2012**, *5*, 367.
- (18) Lindorff-Larsen, K.; Piana, S.; Palmo, K.; Maragakis, P.; Klepeis, J. L.; Dror, R. O.,

- Shaw, D. E. Improved side-chain torsion potentials for the Amber ff99SB protein force field. *Proteins*. **2010**, 78.
- (19) Burley, S. K.; Bhikadiya, C.; Bi, C.; Bittrich, S.; Chen, L.; Crichlow, G. V.; Christie, C. H.; Dalenberg, K.; Di Costanzo, L., Duarte, J. M. RCSB Protein Data Bank: powerful new tools for exploring 3D structures of biological macromolecules for basic and applied research and education in fundamental biology, biomedicine, biotechnology, bioengineering and energy sciences. *Nucleic. acids. research*. **2021**, 49, D437-D451.
- (20) Bujacz, A. Structures of bovine, equine and leporine serum albumin. *Acta. Cryst.* **2012**, 68, 1278-1289.
- (21) Jorgensen, W. L.; Chandrasekhar, J.; Madura, J. D.; Impey, R. W., Klein, M. L. Comparison of simple potential functions for simulating liquid water. *J. Chem. Phys.* **1983**, 79, 926-935.
- (22) Zhong, C. See <https://gitee.com/coordmagic/coordmagic.git>.
- (23) Tawada, Y.; Tsuneda, T.; Yanagisawa, S.; Yanai, T., Hirao, K. A long-range-corrected time-dependent density functional theory. *J. Chem. Phys.* **2004**, 120, 8425-8433.
- (24) Wang, E.; Sun, H.; Wang, J.; Wang, Z.; Liu, H.; Zhang, J. Z. H., Hou, T. End-point binding free energy calculation with MM/PBSA and MM/GBSA: Strategies and applications in drug design. *Chem. Rev.* **2019**, 119, 9478-9508.